# SimoBot: An Underactuated Miniature Robot Driven by a Single Motor

Yifan Zhang, Renjie Zhu, *Graduate Student Member, IEEE*, Jianhao Wu, and Hongqiang Wang, *Member, IEEE*

***Abstract*— A simple-structured, low-cost miniature robot is highly desired for swarm robotics research. In this article, we designed an underactuated miniature robot using only one motor, named as SimoBot, to save space, cost, weight, and energy consumption. Since it has only one motor but needs to travel on the 2-D ground, the design, moving mechanism, and control are all challenging. We conceived a movement strategy based on the interplaying between the centrifugal force and swinging motion of the robot to generate translation and rotation on the ground and finally follow various arbitrary paths. This robot has only five simple components—a vibration motor, a button cell, a microcontroller board, four-pin legs (one of which is shorter than the others), and sensors. This article built the kinematics and kinetics models and analyzed and optimized the parameters. The prototype weighs only 4.76 g, costs 4.7 dollars, and is 20 mm in diameter and 18 mm in height. It can run as fast as 40 mm/s. Its cost of transportation is only 55, smaller than most miniature robots with onboard power and insects. By modulating voltage polarities on the motor and the periods, we demonstrated the controllability of SimoBot by the movement along a straight line, a circle, an "S" curve, and more arbitrary trajectories.**

Manuscript received 12 June 2021; revised 14 November 2021 and 26 April 2022; accepted 6 May 2022. Recommended by Technical Editor S. Mohan and Senior Editor G. Alici. This work was supported in part by the National Natural Science Foundation for Young Scientists of China under Grant 51905256, in part by the Natural Science Foundation of Guangdong Province of China under Grant 2020A1515010955, in part by the Science, Technology and Innovation Commission of Shenzhen Municipality under Grant ZDSYS20200811143601004, in part by the Natural Science Foundation of Liaoning Province of China (State Key Laboratory of Robotics joint funding, under Grant 2021-KF-22-11), and in part by the Southern Marine Science and Engineering Guangdong Laboratory (Guangzhou) under Grant K19313901. *(Yifan Zhang and Renjie Zhu contributed equally to this work.) (Corresponding author: Hongqiang Wang.)*

Yifan Zhang, Renjie Zhu, and Jianhao Wu are with the Shenzhen Key Laboratory of Biomimetic Robotics and Intelligent Systems, Department of Mechanical and Energy Engineering, Southern University of Science and Technology, Shenzhen 518055, China (e-mail: zhangyifan2007@qq.com; zhurj@mail.sustech.edu.cn; 11711106@mail.sustech.edu.cn).

Hongqiang Wang is with the Shenzhen Key Laboratory of Biomimetic Robotics and Intelligent Systems, Department of Mechanical and Energy Engineering, Southern University of Science and Technology, Shenzhen 518055, China, also with the Guangdong Provincial Key Laboratory of Human-Augmentation and Rehabilitation Robotics in Universities, Southern University of Science and Technology, Shenzhen 518055, China, and also with Southern Marine Science and Engineering Guangdong Laboratory, Guangzhou 510000, China (e-mail: wanghq6@sustech.edu.cn).

Color versions of one or more figures in this article are available at https://doi.org/10.1109/TMECH.2022.3189218.

Digital Object Identifier 10.1109/TMECH.2022.3189218

***Index Terms*—Mechanism design, miniature robots, swarms, underactuated robots.**

## I. Introduction

A FLOCK composed of vast numbers of members in nature can robustly accomplish complex tasks that an individual cannot do reliably. For instance, the army ants can build construction of several meters high, while a single ant measures just several millimeters long [1]. A molecule is simple, but by combining into a multicellular organism, multiple molecules together generate complex functions. Nature offers enough clues for robotics that we can achieve a significant power or complexity from a large number of cheap and imprecise individuals [2]. Many researchers have dedicated themselves to this field, although implementing a large number of robots is challenging both in physics and algorithms [3]–[10]. For example, the miniature robot, Kilobot, was designed for studies on swarms, using two vibration motors [11]. The particle robots realize their size expansion and reduction through a complex linkage mechanism to control the connection and release of the surrounding robots and move directionally using the light intensity gradient of the environment [12]. The Smarticle swarm robot has two swing arms driven by servo motors. When multiple Smarticles are placed in a circle to perform a random movement, the whole group can be controlled to move directionally [13].

To save the setup cost and space and improve the robustness of the robot, one of the available solutions is to simplify and miniaturize the mechanical chassis [14]. Among the hardware components, the actuators are a critical part of providing motions and take up most of the robot's cost, energy consumption, and weight [12], [15]–[17]. When the actuator numbers are equal to the system's degrees of freedom (DOFs), this machine is fully actuated. The robot capable of freely running on the ground needs three DOFs and three actuators for full actuation. If the actuator number is less than the DOFs of the system, the robot is underactuated [18]. Underactuated systems can generate complex motions with fewer actuators to save energy, cost, and space, becoming a popular solution for many robots. Most previous swarm robots are underactuated and driven by two actuators, such as the famous Kilobot [11].

Can we further reduce the number of actuators of a swarm robot to the ultimate value (only one) to cost less budget (more agents in the swarm under limited costs) and less maintenance (less labor for usage), lower weight, and less energy consumption (longer running time)? Grand challenges exist in both the locomotion mechanism and control methods. In this article, we proposed a novel mechanical structure for the chassis design

TABLE I
COMPARISON OF EXISTING SWARM ROBOTS, MINIATURE ROBOTS, AND SIMOBOT

| Robot name | Propulsion system | Mass (g) | Dimension (mm) | Speed (mm/s) | Speed (body length/s) | Cost | Categories | |
|---|---|---|---|---|---|---|---|---|
| | | | | | | | Swarm robot | Miniature robot |
| Kilobot [11] | Vibration motors | - | 33 (diameter) | 10 | 0.3 | $ 14.05 | ✓ | ✓ |
| Particle robot [12] | Servo motor | 576 | 155-235 (diameter) | - | - | - | ✓ | |
| Smarticle [13] | Servo motor | 34.8 | 151 (length) | - | - | - | ✓ | |
| HAMR [14] | Piezoelectric | 1.4 | 45.1 (length) | 455.5 | 10.1 | - | | ✓ |
| E-puck [15] | Stepper motors | - | 75 (diameter) | 150 | - | € 250 | | ✓ |
| Jasmine [16] | DC motors | - | 30 × 30× 20 | - | - | - | ✓ | ✓ |
| GRITSBot [17] | Stepper motor | - | 31×30 (foot print) | 250 | 8.1 | $ 46.72 | ✓ | ✓ |
| LPMR [19] | Piezoelectric | 3 | 50×10×9 | 140 | 2.8 | - | | ✓ |
| HoverBot [20] | Planar coils | 19.4 | 39 (diameter) | 6.4 | 0.2 | $ 1.96 | ✓ | ✓ |
| **SimoBot** | **Vibration motor** | **4.76** | **20 (diameter)** | **40[a]** | **2** | **$ 4.70** | ✓ | ✓ |

[a]This velocity refers to the maximum velocity when the robot's trajectory fits a straight line.


Fig. 1. SimoBot. (a) Prototype compared with a human finger as a reference. (b) Components of the robot, including a vibration motor, a button cell, a control board, and the four legs made from two staples (sensors are optional, which are not shown here).

and locomotion mechanism and devised a single-motor robot named "SimoBot." The robot is driven by a coin vibration motor with a cam rotor inside. The legs of the robot are of different lengths, and hence the robot swings corresponding to the rotor's position and centrifugal force. The robot can translate and rotate simultaneously, resulting from the centrifugal force from the rotor and the swinging motion. By intentionally controlling the moving directions and paths, the robot can follow various arbitrary paths consequently.

A typical prototype is composed of only five components: a coin vibration motor for locomotion, a button cell as the power supply, a microcontroller board, sensors, and four legs, as shown in Fig. 1. It is only 20 mm in diameter and 15 mm high, smaller than most of the other similar microrobots and swarm robots [11]–[17], [19], [20], as listed in Table I. The robot can run as fast as 40 mm/s (two body length per second, see Video S1). Since the robot is based on only five off-the-shelf simple parts, the cost is low, only 4.7 dollars. It is one of the smallest swarm robots and comparable with most other miniature robots in the aspects of size, weight, and speed, as shown in Table I. Due to the lightweight and the small number of motors, the robot is energy efficient [Cost of transport (CoT): 55, smaller than most miniature robots and insects], and it can work for more than 85 min with a battery of 50 mAh.

The contributions of this article are threefold: 1) designing the mechanical structure for the miniature underactuated robot using only a single motor; 2) conceiving the moving mechanism and building the mathematical model, path planning, and control method; and 3) devising a prototype, characterizing its motor speed, force, the diameter of the basic circle, and energy consumption, and demonstrating its controllability by following arbitrary paths.

The rest of this article is as follows. The next section introduces the mechanical structure design, the kinematic and kinetics modeling, and the parametric analyses. Section III describes the path planning of the robot. Section IV explains the fabrication and assembly of SimoBot. In Section V, we describe the process and results of the experiments. Finally, Section VI concludes this article.

## II. DESIGN AND MODELING OF THE MECHANICAL CHASSIS

### A. Mechanical Design

To have a simple locomotion mechanism, small size, and low cost, we determined to design the robot based on the stick-slip mechanism [21], [22]. With this mechanism, no transmission mechanism exists since the motion of the robot is generated by the unbalanced force of the motor, hence transmission components are few. To generate the unbalanced force, we utilize only one vibration motor as the power source, while previous similar swarm miniature robots usually employ motors of more than two [11]. A typical vibration motor contains three primary parts: a stator, a rotor, and an eccentric mass. The rotor is driven by an alternating electromagnetic field to spin along a shaft. The eccentric mass is fixed to the rotor shaft. The rotating eccentric

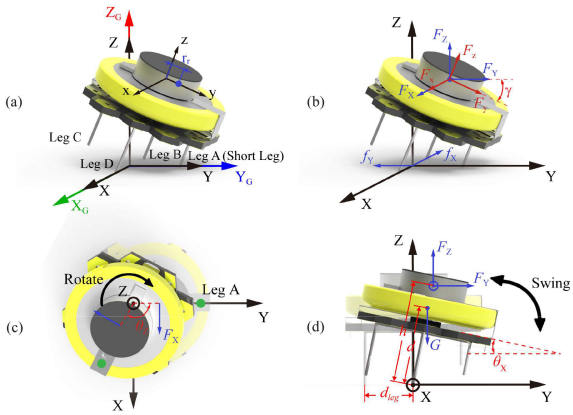


Fig. 2. Coordinate system definition and load distribution. (a) Cartesian coordinate systems in robot modeling. (b) Forces on the robot resulting in translation on the *XY* plane. (c) Forces on the robot resulting in rotating around the *Z* axis. (d) Forces on the robot resulting in swinging around the *X* axis.

mass generates a centrifugal force on the robot. The magnitude of the centrifugal force is constant if the angular speed of the rotor is constant, but the direction of the force varies periodically.

To move freely on a horizontal plane, the robot should be subject to in-plane orthogonal force components and torque along the vertical axis. If the centrifugal force is isotropic in different directions, the robot moves forward and backward at the same distance, consequently without any displacement (i.e., the mean speed is zero). Moreover, little torque is generated from the vibration motor directly, making the robot's turning difficult. To circumvent these challenges, we initially keep the robot erect at the ground, place the vibration motor at a horizontal plane (the rotor shaft is vertical), and intentionally shorten one of the four legs. Due to the force balancing between weight, centrifugal force, and supporting force, the robot changes its gestures at moments—from erecting to tilting and vice versa. The tilted motor results in the discrepancy of the vertical components of centrifugal force between the forward and backward movements and a directional translation of the robot.

Meanwhile, the centrifugal force generates torque with the friction force and robot rotation. Consequently, the robot can run on a circle path if the motor keeps spinning at a constant speed. The detailed kinematic and kinetic analyses are in the next part.

## B. Kinematics and Kinetics Analyses

As shown in Fig. 2(a), we established three Cartesian coordinate systems. The coordinate system $xyz$ is fixed on the vibration motor. The coordinate system $XYZ$ moves with the robot body, in which the line from leg *B* to *D* is the $X$ axis, the center of the legs is the origin, and the $XY$ plane is horizontal. $X_GY_GZ_G$ is the global coordinate system, and it is overlapped with *XYZ* initially.

The vibration motor is a dc motor, and thus we have

$$\omega_r = kV \tag{1}$$

where $V$ is the input voltage and $k$ is the ratio. The centrifugal force from the rotor and the eccentric mass is

$$F = m_r\, r_r \omega_r^2 \tag{2}$$

where $m_r$ is the mass of the rotor and eccentric mass, $r_r$ is the distance between the gravity center of the rotor and eccentric mass and the $z$ axis, and $\omega_r$ is the rotational speed of the vibration motor. Assuming the rotational angle of the rotor starts from zero, at the time $t$ , it becomes

$$\theta_z = \omega_r\, t \tag{3}$$

where $\theta_z$ is the rotational angle of the vibration motor around the $z$ axis. Therefore, the centrifugal force in the coordinate system *XYZ*, as shown in Fig. 2(b), can be obtained

$$\begin{bmatrix} F_X \\ F_Y \\ F_Z \end{bmatrix} = \begin{bmatrix} 1 & 0 & 0 \\ 0 & \cos\gamma & -\sin\gamma \\ 0 & \sin\gamma & \cos\gamma \end{bmatrix} \begin{bmatrix} F_x \\ F_y \\ F_z \end{bmatrix} = \begin{bmatrix} -F\sin\theta_z \\ F\cos\theta_z\cos\gamma \\ F\cos\theta_z\sin\gamma \end{bmatrix} \tag{4}$$

where $F_x$, $F_y$, and $F_z$ are the components of the centrifugal force $F$ in the $x$, $y$, and $z$ directions, respectively, $\gamma$ is the maximum inclination angle of the vibration motor, and $F_X$, $F_Y$, and $F_Z$ are the components of the centrifugal force $F$ in the $X$, $Y$, and $Z$ directions, respectively [Fig. 2(b)]. $F_{XY} = [F_X, F_Y]$ is the component force obtained by decomposing the centrifugal force $F$ in the $XY$ plane. Initially ($t = 0$) the direction vector is $[0, \cos\gamma]$ and at the time $t$, the direction vector of $F_{XY}$ is $[-\sin\theta_z, \cos\theta_z\cos\gamma]$. Therefore, the angle between these two direction vectors is the robot rotation angle, and we have such relationships

$$|\cos\theta_{XY}| = \frac{\cos\gamma}{\sqrt{\tan^2\theta_z + \cos^2\gamma}} \tag{5}$$

$$|\sin\theta_{XY}| = \frac{\tan\gamma}{\sqrt{\tan^2\theta_z + \cos^2\gamma}}\,. \tag{6}$$

When the robot moves on the ground, the friction force is

$$f_{XY} = \mu\,(mg - F_Z) \tag{7}$$

where $\mu$ is the coefficient of friction between the robot and ground, and $m$ is the mass of the robot. Its components at the $X$ and $Y$ axes are, respectively

$$f_X = -f_{XY}\sin\theta_{XY} \tag{8}$$

$$f_Y = f_{XY}\cos\theta_{XY}. \tag{9}$$

The robot is subject to both the centrifugal force and the friction force on the $XY$ plane [Fig. 2(b)]. Here, we assumed the coefficient of static friction is the same as the dynamic friction coefficient. When the robot is moving, the direction of the friction force is opposite to the direction of its speed. When the robot is at rest, if the centrifugal force is greater than the friction force, the direction of the friction force is opposite to the direction of centrifugal force. If the centrifugal force is less than the maximum static friction force, the friction force is the reaction force of the centrifugal force (same magnitude but opposite direction). Hence, the accelerations of the robot in the $X$ and $Y$ directions can be obtained as follows, respectively

$$a_X = \begin{cases} \frac{F_X - \mathrm{sign}(v_X)|f_X|}{m} & when\ v_X \neq 0 \\ \frac{F_X - \mathrm{sign}(F_X)|f_X|}{m} & when\ v_X = 0 \text{ and } |F_X| \geq |f_X| \\ 0 & when\ v_X = 0 \text{ and } |F_X| < |f_X| \end{cases} \tag{10}$$

$$a_Y = \begin{cases} \frac{F_Y - \text{sign}(v_Y)|f_Y|}{m} & when\ v_Y \neq 0 \\ \frac{F_Y - \text{sign}(F_Y)|f_Y|}{m} & when\ v_Y = 0 \text{ and } |F_Y| \geq |f_Y| \\ 0 & when\ v_Y = 0 \text{ and } |F_Y| < |f_Y| \end{cases} \cdot \tag{11}$$

As shown in Fig. 2(c), on the *XY* plane, the robot can rotate around the $Z$ axis since it is also affected by centrifugal torque $M_Z$ and friction torque $M_{rZ}$. They can be obtained as follows, respectively

$$M_Z = F_X\ h \sin\theta_X \tag{12}$$

$$M_{rZ} = f_{XY}\ d_{\text{leg}} \tag{13}$$

where $h$ is the distance between the origins of coordinate system $xyz$ and *XYZ*, $d_{\text{leg}}$ is the distance between the robot's leg and the $Z$ axis at the initial status.

Similar to the acceleration in $X$ and $Y$ directions, when the robot is rotating, the direction of the friction torque is opposite to the direction of rotation. When the robot is stationary, and the centrifugal torque is greater than the friction torque, the direction of the friction torque is opposite to the centrifugal force. In other cases, the angular acceleration is zero. Hence, the angular acceleration can be expressed by

$$\alpha_Z = \begin{cases} \frac{M_Z - \text{sign}(\omega_Z)|M_{rZ}|}{J_Z} & when\ \omega_Z \neq 0 \\ \frac{M_Z - \text{sign}(M_Z)|M_{rZ}|}{J_Z} & when\ \omega_Z = 0 \text{ and } |M_Z| \geq |M_{rZ}| \\ 0 & when\ \omega_Z = 0 \text{ and } |M_Z| < |M_{rZ}| \end{cases} \tag{14}$$

where $J_Z$ is the moment of inertia of the robot around the $Z$ axis.

Based on our observation, Leg *B* and *D* always contact the ground during the movement, but Leg *A* and *C* touch the ground for a short time and then bounce out [Fig. 2(d)]. Thus, we only consider two legs (Leg *B* and *D*) to contact the ground in the above calculation. With such rotational acceleration, the robot spins on the ground. By combing the translation and rotation on the ground, the robot consequently moves on an arc.

Meanwhile, in the $YZ$ plane, the robot is subjected to the torque generated by the gravity and centrifugal force, which makes the robot swing along the $X$ axis, as shown in Fig. 2(d). The angular acceleration around the $X$ axis is

$$\alpha_X = \begin{cases} \frac{F_Y h \cos\theta_X + (mgd - F_Z h)\sin\theta_X}{J_X} & when\ 0 \leq \theta_X \leq \gamma \\ 0 & else \end{cases} \tag{15}$$

where $d$ is the distance between the robot gravity center and the origin of *XYZ*, and $J_X$ is the moment of inertia of the robot around the $X$ axis.

### C. Trajectory Modeling

We estimated the robot's trajectory in the global coordinate system. In the beginning, the robot is at rest

$$a_X\ (0) = a_Y\ (0) = \alpha_X\ (0) = \alpha_Z\ (0) = 0 \tag{16}$$

$$v_X\ (0) = v_Y\ (0) = \omega_X\ (0) = \omega_Z\ (0) = 0 \tag{17}$$

$$X_G\ (0) = Y_G\ (0) = Z_G\ (0) = \varphi_Z\ (0) = 0. \tag{18}$$

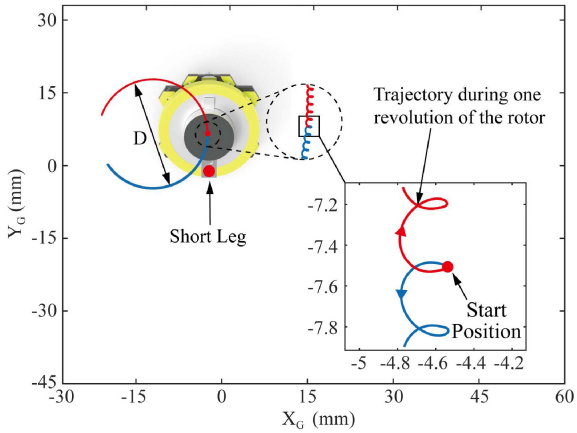


Fig. 3. Movement of the robot on the $X_G Y_G$ plane. The basic trajectory circle is generated by the robot, while the rotor continuously spins at a constant speed. The red and blue curvatures represent that SimoBot's motor is driven by positive and negative voltage and SimoBot rotates in counterclockwise and clockwise directions, respectively. The spiral line is the trajectory during one revolution of the rotor.

During an incremental time, $\Delta t$, the speed of the robot can be regarded as a constant. Then, the displacement and rotational angle can be

$$\Delta X\ (i) = v_X\ (i)\ \Delta t \tag{19}$$

$$\Delta Y\ (i) = v_Y\ (i)\ \Delta t \tag{20}$$

$$\Delta\varphi_X\ (i) = \omega_X\ (i)\ \Delta t \tag{21}$$

$$\Delta\varphi_Z\ (i) = \omega_Z\ (i)\ \Delta t. \tag{22}$$

At the $i$th iteration, the speed can be calculated from the acceleration of the robot

$$v_X\ (i) = v_X\ (i-1) + a_X\ (i-1)\ \Delta t \tag{23}$$

$$v_Y\ (i) = v_Y\ (i-1) + a_Y\ (i-1)\ \Delta t \tag{24}$$

$$\omega_X\ (i) = \begin{cases} \omega_X(i-1) + \alpha_X(i-1)\Delta t & when\ 0 \leq \varphi_X(i-1) \leq \gamma \\ 0 & else \end{cases} \tag{25}$$

$$\omega_Z\ (i) = \omega_Z\ (i-1) + \alpha_Z\ (i-1)\ \Delta t. \tag{26}$$

Then, the position and the angle of the robot in the global coordinate system can be obtained

$$X_G\ (i) = X_G\ (i-1) + \Delta X\ (i)\cos\left(\Delta\varphi_Z\ (i)\right) + \Delta Y\ (i)\sin\left(\Delta\varphi_Z\ (i)\right) \tag{27}$$

$$Y_G\ (i) = Y_G\ (i-1) + \Delta Y\ (i)\cos\left(\Delta\varphi_Z\ (i)\right) - \Delta X\ (i)\sin\left(\Delta\varphi_Z\ (i)\right) \tag{28}$$

$$\varphi_Z = \sum \Delta\varphi_Z\ . \tag{29}$$

With the above equations, we can estimate the robot's trajectory through iteration. The results are shown in Fig. 3. The parameters correspond to our prototype's specifications (Table II). After the rotor spins for one revolution counterclockwise (CCW), the robot's trajectory forms a short spiral arc. The trajectory generated during each rotor revolution is the same—a complex circular spiral curve. If the rotor reverses the rotation

TABLE II
PARAMETERS USED IN THE ESTIMATION

| Parameters | Value |
|---|---|
| $m_r$ | $2.50 \times 10^{-4}$ kg |
| $r_r$ | $1.54 \times 10^{-3}$ m |
| $\omega_r$ | 3600 r/min |
| $\gamma$ | 30° |
| $\mu$ | 0.3 |
| $m$ | $4.76 \times 10^{-3}$ kg |
| $h$ | $1.20 \times 10^{-2}$ m |
| $d$ | $1.05 \times 10^{-2}$ m |
| $J_X$ | $8.17 \times 10^{-7}$ kg · $m^2$ |
| $J_Z$ | $2.08 \times 10^{-7}$ kg · $m^2$ |
| $d_{leg}$ | 0.01 m |
| $\Delta t$ | $10^{-4}$ s |

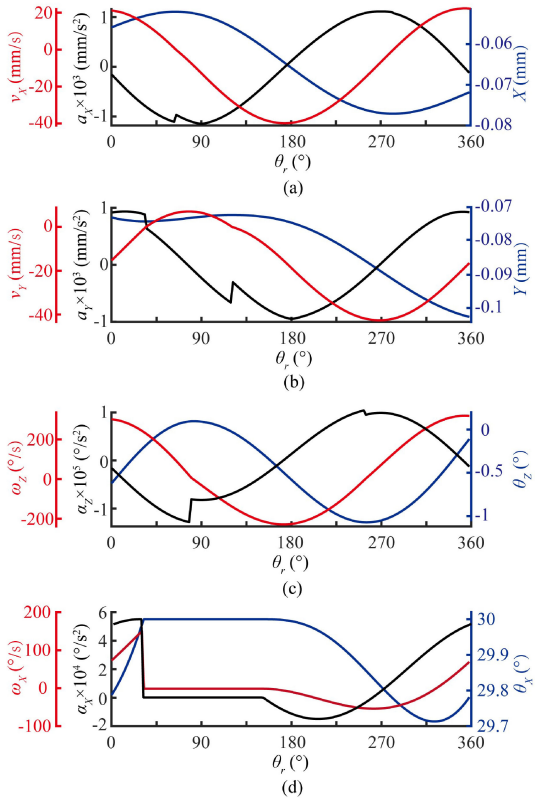


Fig. 4. Parameters' variance including (a) acceleration, velocity, and displacement on the *X* axis and (b) on the *Y* axis, and (c) angular acceleration, angular velocity, and rotational angle along the *Z* axis and (d) along the *X* axis, during one revolution of the rotor.

direction, this trajectory keeps the same shape but in the opposite direction. By repeating the rotation of the rotor, the spiral arcs connect each other in a series, and consequently generate a big circle trajectory (named the basic trajectory circle since it is the elementary movement route) with a diameter *D*.

The translation on the *XY* plane and the rotation around the *X* and *Z* axes during one stable rotor revolution are displayed in Fig. 4. Some discontinuities happen on the acceleration, which

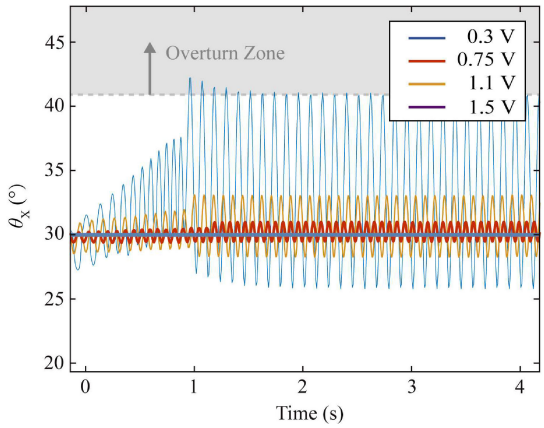


Fig. 5. Swinging degree along the *X* axis of SimoBot on different voltages of motor.

is caused by the nonlinear friction force and impact with the ground, according to (10)–(15). For example, in Fig. 4(a), for $\theta_r$ less than 60 ° , the robot is braking (the velocity is positive, but the acceleration is negative) with the net force of the centrifugal force $F_X$ and the friction force $f_X$, i.e., $(F_X + |f_X|)$. However, when the velocity becomes negative, the centrifugal force accelerates the robot, but the friction force still resists the movements, with which the net force becomes $(F_X - |f_X|)$. Therefore, the acceleration is discontinuous. Similar phenomenon happens in the translation at the *Y* direction and the rotation along the *Z* axis as shown in Fig. 4(b) and (c), respectively. On another hand, the rotation along the *X* axis faces the impact with the ground, which results in a discontinuous force and acceleration. Here, we assume the velocity becomes zero once the robot contacts the ground. In the above model, the hypotheses about the friction force and impact might result in errors in estimation, but in the current stage they can be accepted according to the experimental results, and the driving accuracy can be improved further by closed-loop control in the future.

With the above equations, we analyze the parameters, including the input voltage on the motor (V), the motor speed ($\omega_r$), the robot mass ($m$), initial inclination angle ($\gamma$), the coefficient of friction ($\mu$), the length of legs ($L_{\text{leg}}$), and the horizontal distance of the legs ($d_{\text{leg}}$) to optimize the design and control of the robot. Based on the models, if the input voltage is too small (e.g., 0.3 V), the robot's driving force is not enough to overcome the frictional force, so the robot maintains an initial angle, 30° (the straight line in Fig. 5) and cannot move. On the contrary, if the voltage is too high (e.g., 1.5 V), the centrifugal force is too strong and might overturn the robot (i.e., $\theta_X > 41°$) after several rotor revolutions.

In the analysis, we set the ratio ($k$) as 4583.2, according to the preliminary tests on the motor used in the prototype.

As shown in Fig. 6, higher $\omega_r$ increases *D*. When $\omega_r$ is approximately 4400 and 5500 rpm, the robot's speed and angular speed reach the peaks, respectively. Lower rotor speed $\omega_r$ reduces both the linear and angular robot speeds since the centrifugal force is smaller. When $\gamma$ is approximately 62°, the average linear speed arrives at the maximum, while the angular speed peaks when $\gamma$ is approximately 22°. The greater $\gamma$ monotonously decreases the diameter *D*. As for the increasing coefficient of friction $\mu$, as shown in Fig. 6(c), the diameter drops continuously, the linearly

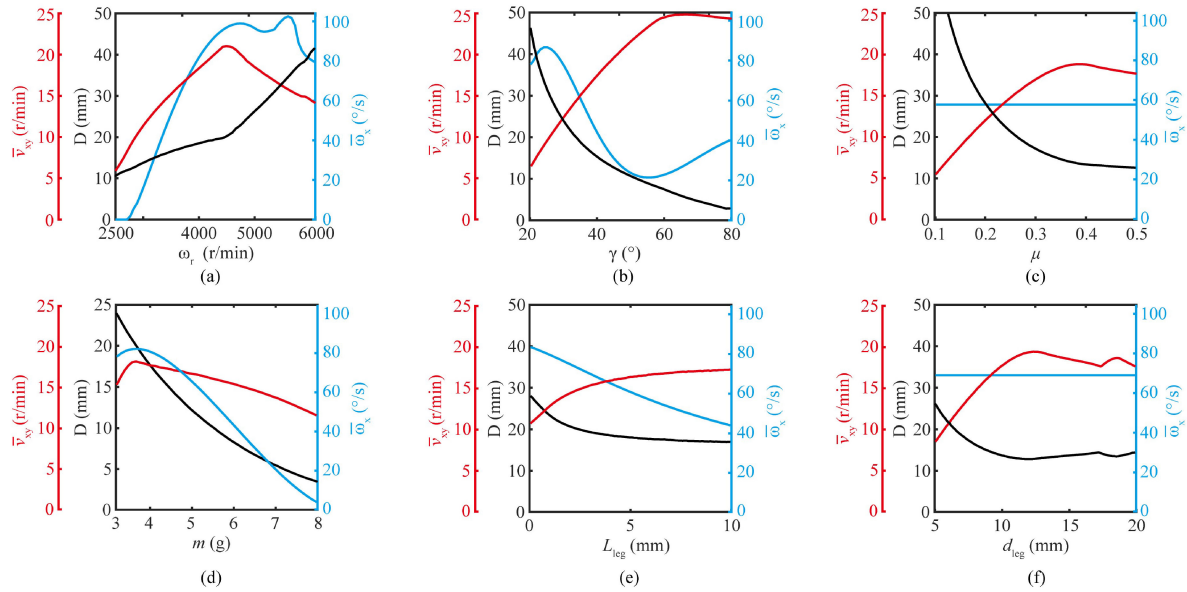


Fig. 6. Effects of different factors on robot performance, including (a) motor speed, (b) initial inclination angle, (c) coefficient of friction, (d) robot mass, (e) the length of legs, and (f) horizontal distance between the legs.

speed peaks when $\mu$ is approximately 0.38, but the angular speed keeps constant. The mass of robot generates the maximum linear and angular speed when $m$ is 3.5 and 3.8, respectively; larger mass results in smaller diameter, as shown in Fig. 6(d). On another aspect, with the longer length of the legs, both the diameter and angular speed reduce, but the linear speed rises. $d_{\text{leg}}$ does not influence the angular speed, and increases and decreases the linear speed and diameter, respectively. In summary, when $\omega_r$ is about 4400 rpm, $\gamma$ is 60°, $\mu$ is approximately 0.4, $m$ is around 3.5 g, and $d_{\text{leg}}$ is 12 mm, respectively, the robot's speed reaches a peak, but the change of $L_{\text{leg}}$ has little effect on the average translation speed. When $\gamma$, $\mu$, $L_{\text{leg}}$, and $d_{\text{leg}}$ tend to zero, the trajectory diameter of the robot ($D$) is infinite. The increase of these parameters declines $D$. When the average rotational speed $\bar{\omega}_X$ around the $X$ axis is higher, the impact force is greater when the Leg $A$ and $C$ contact the ground, so this parameter is closely related to the smoothness of the robot's movements, and it cannot be very large. When the motor speed increases, $\bar{\omega}_X$ gradually increases. $\mu$ and $d_{\text{leg}}$ have no effect on $\bar{\omega}_X$. An increase in the other three parameters results in a decrease in $\bar{\omega}_X$.

## III. Path Planning

As discussed in the last part, the trajectory of the robot is a complex spiral curve during one rotor revolution, and it is roughly a large circle (the basic trajectory circle) if the rotor keeps spinning. Thus, it is difficult to control the robot to run on a straight line or an arbitrary shape. Here, we first translate the aim path into a path composed of arcs that can be followed by the robot. By connecting the arcs from the basic trajectory circle with different lengths and directions, we can fit most of the desired tracks on the ground.

As shown in Fig. 7(a), we can connect arcs of the same length but in different directions in a series. Consequently, the robot's trajectory fits a straight line. The central angle of each arc for clockwise (CW) or CCW traveling are the same. During each arc, the displacement of the robot is

$$L = D\sin\frac{\theta}{2}. \tag{30}$$

On another aspect, if the arc length for one direction is longer than that for the other direction, the final trajectory approximates a large circle [Fig. 7(b)]. Assuming the diameter of basic trajectory circles are $D$, and the central angles are $\theta_1$ and $\theta_2$, respectively, the parameter $\beta$, $a$, $b$, and $c$ can be obtained as

$$\beta = \frac{\theta_1 - \theta_2}{2} \tag{31}$$

$$a = \frac{D}{2}\cos\frac{\theta_1}{2} \tag{32}$$

$$b = \frac{D}{2}\sin\frac{\theta_1}{2} \tag{33}$$

$$c = 2\left[\frac{\frac{D}{2}\sin\frac{\theta_1}{2}\cos\left(\frac{\theta_1-\theta_2}{2}\right)}{\sin\left(\frac{\theta_1-\theta_2}{2}\right)}\right] - \frac{D}{2}\cos\frac{\theta_1}{2}. \tag{34}$$

According to the Pythagorean theorem (yellow right-angled triangle), the diameter of the fitted circle can be obtained as

$$\begin{aligned} D_{\text{fit}} &= 2\,r_{\text{fit}} = 2\sqrt{b^2+c^2} \\ &= \frac{\sqrt{D^2\left[\sin^2\left(\frac{\theta_1}{2}\right)+\sin^2\left(\frac{\theta_2}{2}\right)+2\sin\left(\frac{\theta_1}{2}\right)\sin\left(\frac{\theta_2}{2}\right)\cos\left(\frac{\theta_1-\theta_2}{2}\right)\right]}}{\sin\left(\frac{\theta_1-\theta_2}{2}\right)}. \end{aligned} \tag{35}$$

In this way, more arbitrary trajectory can be implemented, as shown in Fig. 7(c). The basic path planning can be as follows:

1) At first, the robot simply moves on the basic circle.
2) Once it approaches the intersection point between the aim trajectory and the basic circle, the rotor reverses the direction, and the robot moves in the opposite direction of the basic circle.

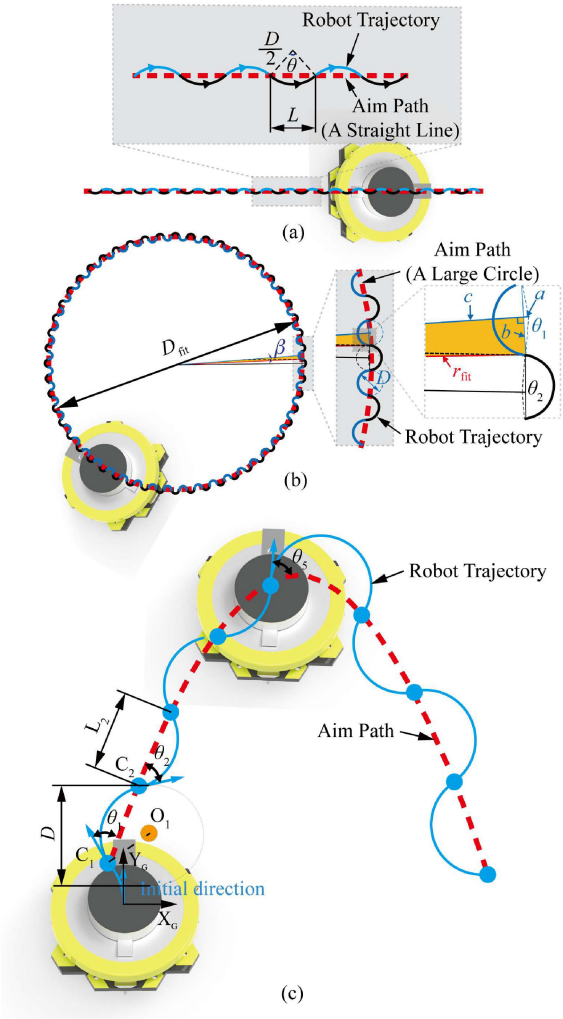


Fig. 7. Path of SimoBot while fitting (a) straight line, (b) large circle, and (c) random curvature, respectively.

3) By repeating the above two steps. Consequently, the robot trajectory can fit the arbitrary path.

Supposing the distance of the two intersection points between the random curvature and the $i$th basic circle is $L_i$, the corresponding traveling angle on this circle is

$$\theta_i = \begin{cases} 2\arcsin\left(\frac{L_i}{2D}\right), & when\ \theta < \frac{\pi}{2}; \\ 2\pi - 2\arcsin\left(\frac{L_i}{2D}\right), & when\ \frac{\pi}{2} < \theta < \pi. \end{cases} \tag{36}$$

However, since the SimoBot's trajectory is combined by arcs of different lengths, discrepancy always exists between the aim path and the robot trajectory. The error can be as large as the radius of the basic circle, e.g., when the path has a sharp turn. This error can be reduced by shortening the arcs, with the tradeoff on the average velocity due to more frequent switching of the motor directions.

## IV. Implementation of SimoBot

### A. Mechanical Structure

SimoBot is made of only four parts, except for the optional sensor part: a vibration motor for motion output, a button cell as power supply, a control board for robot control, four legs, and sensors (optional), as shown in Fig. 1(b). The vibration motor (TELESKY 1027) is mounted on the on-board circuit (CheapDuino), and the button cell (LIR2032, 50 mAh), as shown in Fig. 8. The legs are made from staples (Comix B3054 24/8, 12 × 8 mm), and one of them is a little shorter than the others (the shorter one: 5 mm; others: 8 mm) on purpose. These components are glued together instead of using screws and bolts to reduce the size and the number of components and facilitate the assembly process. The total weight of the robot is only 4.76 g (except the sensors, which are optional depending on the application scenarios).

All the components of SimoBot are mass-produced, and hence their cost and quality are ensured. The total hardware cost of SimoBot is only $ 4.70, except the sensors (optional), as shown in Fig. 9, much lower than most other miniature robots and swarm robots.

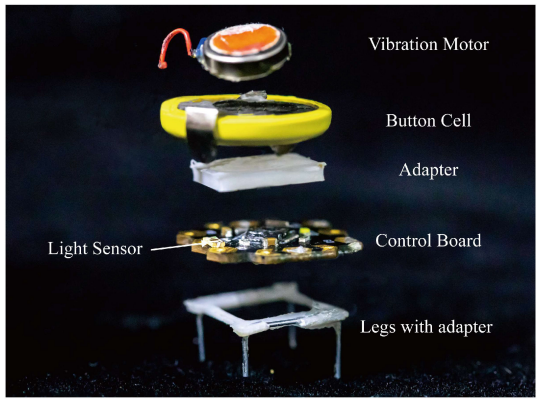


Fig. 8. Exploded view of SimoBot.


Fig. 9. Mass and cost contribution of each component of SimoBot.

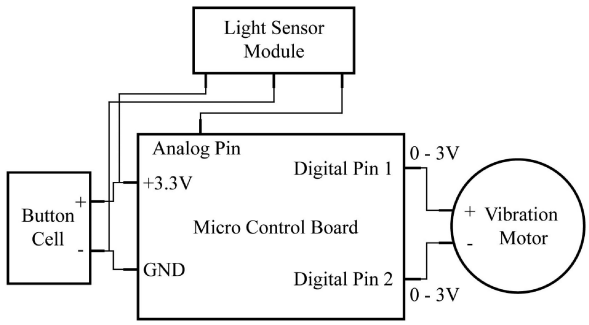


Fig. 10. Schematic diagram of the control circuit.

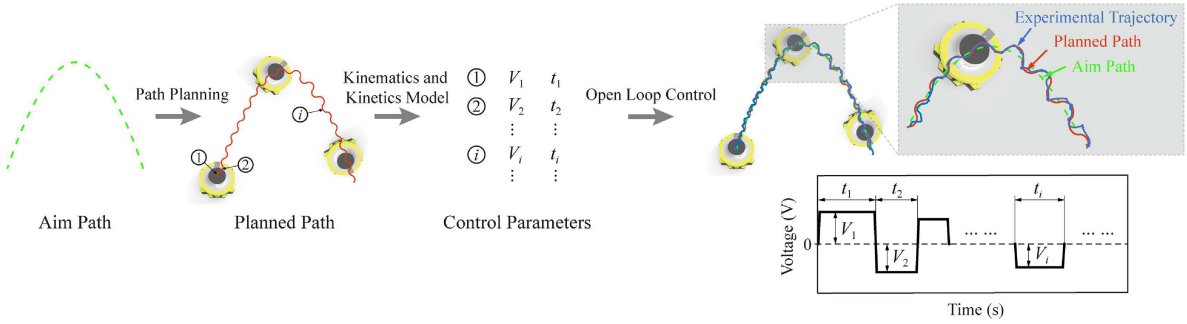


Fig. 11. Control method of SimoBot following arbitrary trajectories.

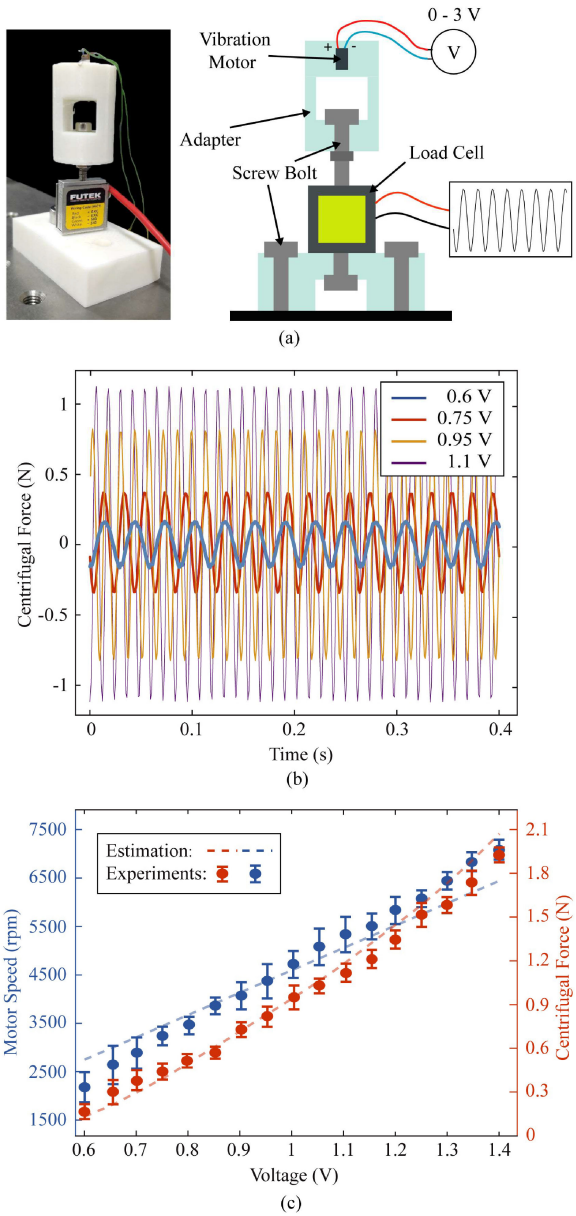


Fig. 12. Measurement of motor speed. (a) Measurement setup. (b) Centrifugal force of the motor while the motor is powered ON. (c) Motor speeds and centrifugal force on different voltages.

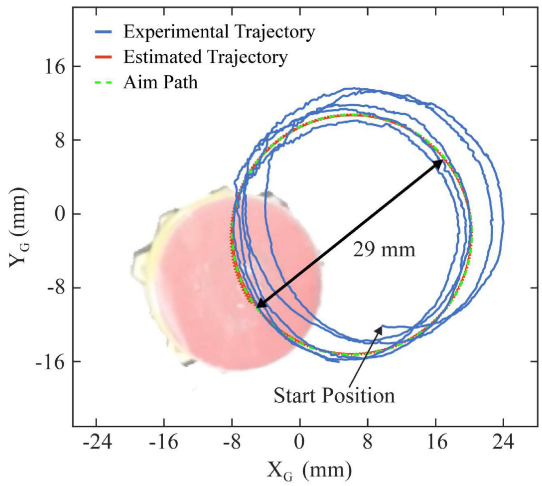


Fig. 13. Trajectories of SimoBot during a long term when the voltage is constant (1.1 V).

## B. Electrical Circuit

As shown in Fig. 10, the button cell is connected to the microcontrol board to support the electrical energy (3.3 V). Two digital pins of the micro control board with PWM output are connected to the vibration motor. Turning ON and OFF the digital pins can control the motor to run and stop, respectively. When digital pin 1 generates a higher voltage than digital pin 2, the rotor rotates CW, while the rotor rotates CCW if the digital pin 2 has a higher voltage. By tuning the voltage of the digital pins, we can follow various paths. The control board has extra four output pins and four input pins available for accessory sensors and actuators, which might be useful for complex tasks such as environment reception and communication.

## C. Control Method

As aforementioned, it is difficult for the robot to follow a track accurately, we need to convert it into a path suitable for the robot, and then control the robot to run on the path. We established the correspondence between the voltage and speed of the vibration motor and the diameter of the basic circle. We can connect the arcs of the basic circle to fit an arbitrary path. To control the length of the arcs, we calculated the central angle at first according to (27) and (28), and estimate the practical angle

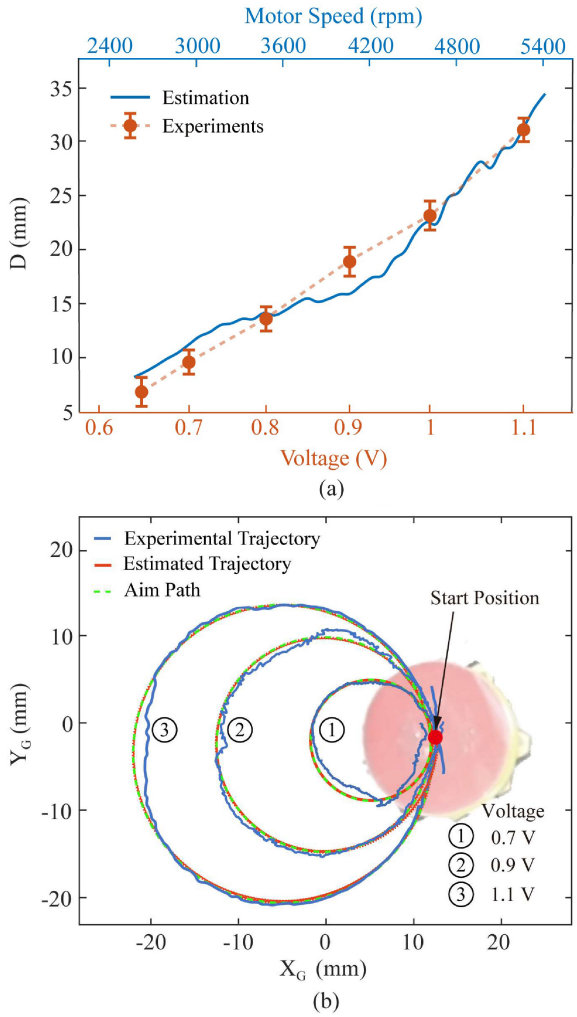


Fig. 14. Diameter of SimoBot's trajectories on different motor speeds and voltages in (a), and the corresponding trajectories of SimoBot when the voltage is 0.7, 0.9, and 1.1 V in (b).

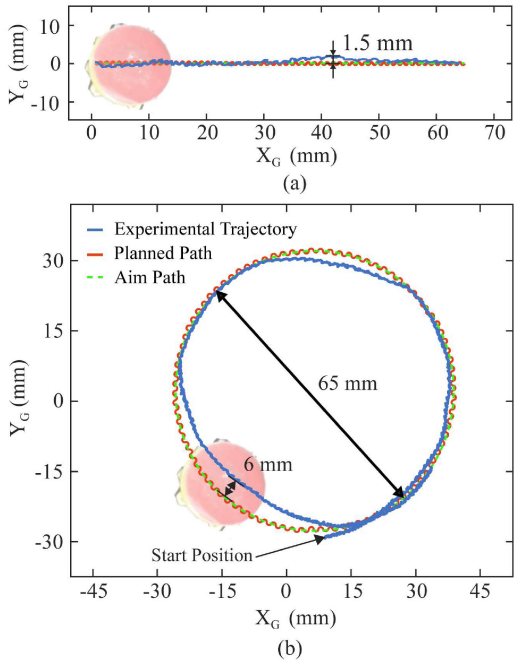


Fig. 15. Trajectories of SimoBot while it controlled to run on a straight line in (a), and a large circle in (b), respectively.

by moving duration (assuming the angular speed is constant). The control method is shown in Fig. 11 and the operation steps are as follows:

*Step 1:* Convert the aim path into a trajectory composed of arcs (at different diameters and lengths) that the robot can run on.
*Step 2:* According to the relationship between the voltage and speed of the vibration motor and the diameter of the basic circle established by the kinematic and kinetics model, determine the driving voltage and time for each arc.
*Step 3:* Sequentially control the motor to run at the specified voltage and time, and finally, SimoBot will follow the arbitrary aim path.

## V. Experiments

### A. Centrifugal Force and Speed of the Motor

The speed and the centrifugal force of the vibration motor at different voltages were tested with the setup [Fig. 12(a)]. The vibration motor was embedded in a three-dimensional printed adapter, and the adapter was connected to a load cell (FUTEK LSB200). The data obtained by the load cell changes over time as a periodical sine function, where the frequency represents the speed of the rotor, and the amplitude represents the vertical components of the centrifugal force in Fig. 12(b). As estimated, the speed increase linearly and the centrifugal force increase exponentially with the voltage in Fig. 12(c). Thus, we can tune the motor speed and centrifugal force simply by differentiating the voltage. The value for the comparison results from at least 10 trials. The little error between the experimental results and estimation might come from the gaps between the motor and the adapter, the temperature changes, and the unstable power supply to the motor. In the experiments, we set voltage among 0.6–1.4 V considering the tradeoff between enough force and overturn.

### B. Basic Features of SimoBot Under a Constant Input Voltage

It is difficult to verify the models by the motions in one rotor revolution due to the quick speed of the rotor (more than 180 r/min) and the small range of movement (tens of micrometers). Here, we validate the model by the robot trajectory during many rotor revolutions, which is easier to observe and more important for the applications.

To verify the models, the robot's basic circular trajectory was tracked by a camera. In the experiments, a marker (a piece of red round paper) was attached to the robot's top, and the robot was driven by a 1.1 V dc voltage. We identified the marker center from the videos by recognizing the color area and matching the shape. The corresponding running trajectories of the robot are shown in Fig. 13. In our test, the robot runs stably for five laps. The root mean square errors were 1.97, 2.76, 1.93, 2.24, and 2.48 mm (2.276 mm on average). After five laps, the robot position drifted by 4.64 mm (the distance between the centers of

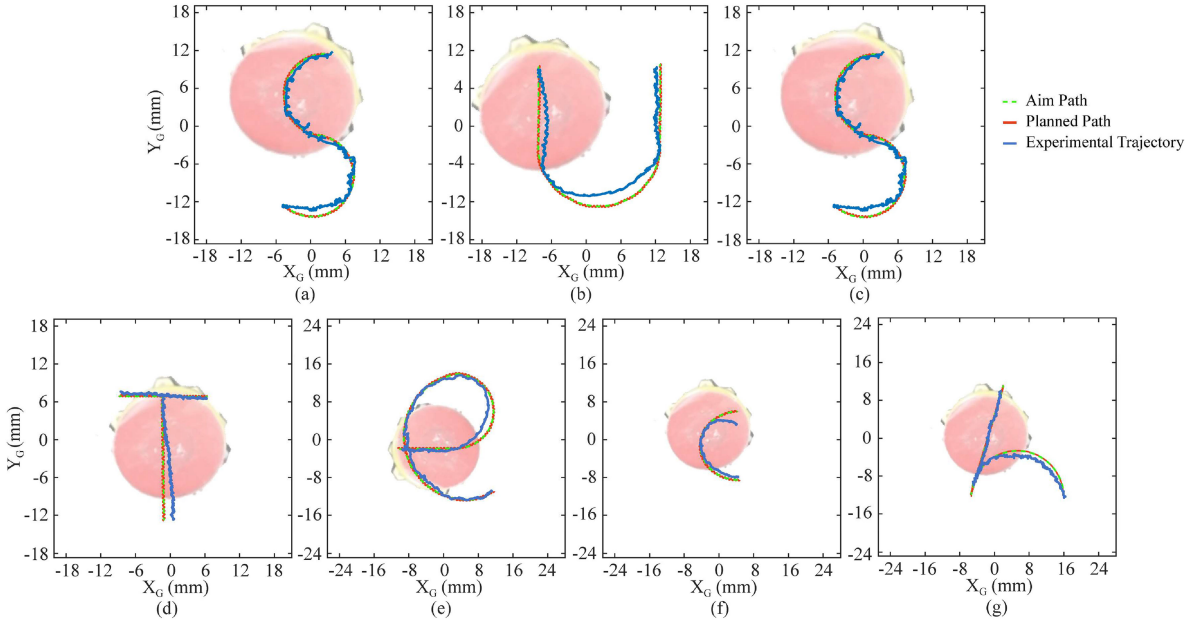


Fig. 16. Trajectories of SimoBot fitting all the alphabets of SUSTech (the authors' affiliation).

the first lap and the last lap). The deviations were mainly caused by the rough surface of the test platform and the variable friction force. These errors can be improved in the future by closed-loop control. As the voltage rises, the basic circle becomes larger (see Fig. 14 and Video S2). The results of experimental and theoretical calculations are roughly the same in tendency. The experimental trajectory has a little error (around 10% of the basic circle diameter) from the aimed track. The differences might come from the position recognition algorithm and the inhomogeneous contact surfaces of the substrate and the robot legs. The traveling accuracy can be improved in the future by adding sensor feedback.

### C. Following Various Paths by Tuning the Voltage

As estimated by the model, we can control the robot to follow various arbitrary paths by connecting the small arcs of the basic circles. Just like the path planning mentioned above, we can repeatedly flip the voltage's polarity on the motor after every 0.4 s to control the robot move short arcs of the same length but in different directions (CW and CCW directions) in turn and finally generated a straight-line route [see Fig. 15(a) and Video S3]. The trajectory error between the practical and simulated paths is 1.5 mm at maximum, only 7.5% of the diameter of the robot.

If the duration for the two different voltage polarities on the motor is different, the robot's final trajectory is no longer a straight line. For instance, when we kept negative dc voltage for a longer period (0.5 s) than the positive voltage (0.4 s), the final trajectory became a circle with a diameter of 65 mm [see Fig. 15(b) and Video S3]. The largest error on the practical trajectory and the aim path became 6 mm due to the error accumulated on the long-running path, less than 10% of the aim trajectory diameter. This error mainly results from the nonhomogeneous roughens of the contact surface and the impact between the robot and ground.

By a similar strategy, the robot can follow a more arbitrary path. For instance, to generate an "S" curvature, as shown in Fig. 16(a) and Video S3, in the beginning, the motor was powered by $+1.0$ V (0.4 s) and then $-1.0$ V (0.5 s). After repeating these steps for 15 s, it was powered by $+1.0$ V (0.5 s) and then $-1.0$ V (0.4 s) repeatedly for 15 s. In addition, the trajectory of "e" is composed of a straight line and two semicircles with different diameters. Similarly, we drove the robot to generate all the alphabets of SUSTech (the authors' affiliation) by combining the robot's basic trajectories, showing the robot's great controllability under open-loop control.

### D. Energy and Cost of Transport

CoT is common metric used to evaluate energy consumption in small-scale robots [23] and is defined as

$$CoT = \frac{U}{mgd} = \frac{P}{mgv} \tag{37}$$

where $U$ is the energy input, $m$ is the mass of the robot, $g$ is the standard gravitational acceleration, and $d$ is the distance traveled of the robot. Here, the energy input $U$ and the distance $d$ can be replaced by the power input $P$ and the moving velocity $v$ , respectively. For SimoBot, the input power is calculated by the input voltage and current, which was monitored by a wattmeter (SEN0291, DFRobot). As shown in Fig. 17(a), when the voltage increases, both the input power and the velocity of SimoBot grow (but at different rates), and the CoT drops to approximately 55. The energetic cost of locomotion of SimoBot is lower than most miniature robots (particularly those with on-board power) and insects [24]–[47] (the feature length of miniature robots is smaller than 10 cm according to [23]), as shown in Fig. 17(b), since SimoBot is driven by only one motor without any mechanical transmission mechanism. Based on our

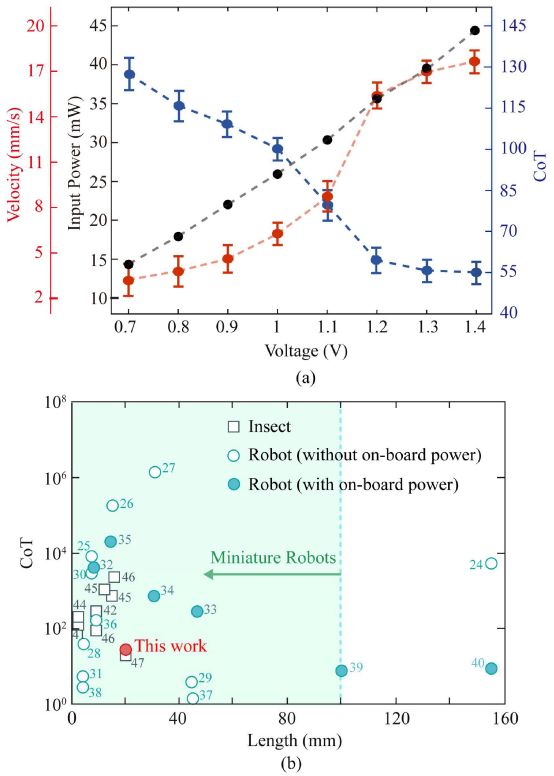


Fig. 17. Energy consumption data of SimoBot. (a) Input power and velocity of SimoBot and its CoT on different voltages. (b) CoT of miniature robots (circles) and insects (squares) plotted against their body masses. The feature length of miniature robots is smaller than 10 cm according to [23].

tests, it can keep running for as long as 85 min with a battery of 50 mAh.

## VI. Conclusion

In this article, we implemented a miniature robot named as SimoBot, which is composed of only five simple components that are glued together. This robot is simple-structured, compact (characteristic length 20 mm), lightweight (4.76 g), low-cost ($ 4.7), and energy-efficient (CoT: 55). Based on the kinematics and kinetics models built in this article, we analyzed and optimized the parameters and propose control strategies. Experiments verify that the consequent motion is a small circle (basic circle) when the motor is driven by a constant dc voltage. By combining the arcs of the basic circle with different lengths and directions, we demonstrated that the robot is capable of running on various aim paths, such as a straight line, a circle, an "S" curve, and more arbitrary shapes.

The control in this article is open-loop, but in the future, by adding sensors and a proper control algorithm (taking the aim path and planned trajectory as references), the robot can be controlled by a closed-loop to improve the locomotion accuracy, and the sensitivity to external disturbances will also be studied. The current article is mainly focused on the design and path planning of a single SimoBot. In the future, communication and cooperation between multiple SimoBots will be studied further.

## References

[1] E. Sahin, "Swarm robotics: From sources of inspiration to domains of application," *Swarm Robot.*, vol. 3342, pp. 10–20, 2004.
[2] M. Brambilla, E. Ferrante, M. Birattari, and M. Dorigo, "Swarm robotics: A review from the swarm engineering perspective," *Swarm Intell.*, vol. 7, no. 1, pp. 1–41, 2013.
[3] F. Arvin, K. Samsudin, and A. R. Ramli, "Development of a miniature robot for swarm robotic application," *Int. J. Elect. Comput. Eng.*, vol. 1, no. 4, pp. 436–442, 2009.
[4] B. V. Johnson, S. Chowdhury, and D. J. Cappelleri, "Local magnetic field design and characterization for independent closed-loop control of multiple mobile microrobots," *IEEE/ASME Trans. Mechatron.*, vol. 25, no. 2, pp. 526–534, Apr. 2020.
[5] H. Xie, X. J. Fan, M. M. Sun, Z. H. Lin, Q. He, and L. N. Sun, "Programmable generation and motion control of a snakelike magnetic microrobot swarm," *IEEE/ASME Trans. Mechatron.*, vol. 24, no. 3, pp. 902–912, Jun. 2019.
[6] M. Noh, S. W. Kim, S. An, J. S. Koh, and K. J. Cho, "Flea-Inspired catapult mechanism for miniature jumping robots," *IEEE Trans. Robot.*, vol. 28, no. 5, pp. 1007–1018, Oct. 2012.
[7] J.-S. Koh, S.-P. Jung, M. Noh, S.-W. Kim, and K.-J. Cho, "Flea inspired catapult mechanism with active energy storage and release for small scale jumping robot," in *Proc. IEEE Int. Conf. Robot. Automat.*, 2013, pp. 26–31.
[8] V. Kopman and M. Porfiri, "Design, modeling, and characterization of a miniature robotic fish for research and education in biomimetics and bioinspiration," *IEEE/ASME Trans. Mechatron.*, vol. 18, no. 2, pp. 471–483, Apr. 2013.
[9] H. Godaba, J. Li, Y. Wang, and J. Zhu, "A soft jellyfish robot driven by a dielectric elastomer actuator," *IEEE Robot. Autom. Lett.*, vol. 1, no. 2, pp. 624–631, Jul. 2016.
[10] J.-S. Koh, S.-p. Jung, R. J. Wood, and K.-J. Cho, "A jumping robotic insect based on a torque reversal catapult mechanism," in *Proc. IEEE Int. Conf. Intell. Robots Syst.*, 2013, pp. 3796–3801.
[11] M. Rubenstein, C. Ahler, and R. Nagpal, "Kilobot: A low cost scalable robot system for collective behaviors," in *Proc. IEEE Int. Conf. Robot. Autom.*, 2012, pp. 3293–3298.
[12] S. Li *et al.*, "Particle robotics based on statistical mechanics of loosely coupled components," *Nature*, vol. 567, no. 7748, pp. 361–365, 2019.
[13] W. Savoie *et al.*, "A robot made of robots: Emergent transport and control of a smarticle ensemble," *Sci. Robot.*, vol. 4, no. 34, 2019, Art. no. eaax4316.
[14] B. Goldberg, N. Doshi, and R. J. Wood, "High speed trajectory control using an experimental maneuverability model for an insect-scale legged robot," in *Proc. IEEE Int. Conf. Robot. Automat.*, 2017, pp. 3538–3545.
[15] F. Mondada *et al.*, "The e-puck, a robot designed for education in engineering," in *Proc. 9th Conf. Auton. Robot Syst. Competitions*, 2009, pp. 59–65.
[16] S. Kernbach, R. Thenius, O. Kernbach, and T. Schmickl, "Re-embodiment of honeybee aggregation behavior in an artificial micro-robotic system," *Adaptive Behav.*, vol. 17, no. 3, pp. 237–259, 2009.
[17] D. Pickem, M. Lee, and M. Egerstedt, "The GRITSBot in its natural habitat-a multi-robot testbed," in *Proc. IEEE Int. Conf. Robot. Automat.*, 2015, pp. 4062–4067.
[18] P. C. Müller and W. Schiehlen, *Linear Vibrations: A Theoretical Treatment of Multi-Degree-of-Freedom Vibrating Systems*. Berlin, Germany: Springer Science & Business Media, 2012.
[19] A. G. Dharmawan, H. H. Hariri, S. Foong, G. S. Soh, and K. L. Wood, "Steerable miniature legged robot driven by a single piezoelectric bending unimorph actuator," in *Proc. IEEE Int. Conf. Robot. Automat.*, 2017, pp. 6008–6013.
[20] M. P. Nemitz *et al.*, "HoverBots: Precise locomotion using robots that are designed for manufacturability," *Front. Robot. AI*, vol. 4, 2017, Art. no. 55.
[21] G. Wang, C. Li, and T. Yuan, "Design and experiment of a small-scale walking robot employing stick-slip motion principle," *Rev. Sci. Instrum.*, vol. 88, no. 11, 2017, Art. no. 115001.
[22] J. Klingner, A. Kanakia, N. Farrow, D. Reishus, and N. Correll, "A stick-slip omnidirectional powertrain for low-cost swarm robotics: Mechanism, calibration, and control," in *Proc. IEEE Int. Conf. Intell. Robots Syst.*, 2014, pp. 846–851.
[23] M. Sitti, *Mobile Microrobotics*. Cambridge, MA, USA: MIT Press, 2017.
[24] M. J. Qi, Y. S. Zhu, Z. W. Liu, X. Y. Zhang, X. J. Yan, and L. W. Lin, "A fast-moving electrostatic crawling insect," in *Proc. IEEE 30th Int. Conf. Micro Electro Mech. Syst.*, 2017, pp. 761–764.
[25] W. A. Churaman, L. J. Currano, C. J. Morris, J. E. Rajkowski, and S. Bergbreiter, "The first launch of an autonomous thrust-driven microrobot using nanoporous energetic silicon," *J. Microelectromech. Syst.*, vol. 21, no. 1, pp. 198–205, 2011.

[26] T. Ebefors, J. U. Mattsson, E. Kälvesten, and G. Stemme, "A walking silicon micro-robot," in *Proc. 10th Int. Conf. Solid State Sensors Actuators*, 1999, pp. 1202–1205.
[27] E. Y. Erdem *et al.*, "Thermally actuated omnidirectional walking microrobot," *J. Microelectromech. Syst.*, vol. 19, no. 3, pp. 433–442, 2010.
[28] D. S. Contreras, D. S. Drew, and K. S. Pister, "First steps of a millimeter-scale walking silicon robot," in *Proc. Int. Conf. Solid-State Sensors, Actuators Microsyst.*, 2017, pp. 910–913.
[29] A. T. Baisch, O. Ozcan, B. Goldberg, D. Ithier, and R. J. Wood, "High speed locomotion for a quadrupedal microrobot," *Int. J. Robot. Res.*, vol. 33, no. 8, pp. 1063–1082, 2014.
[30] J. T. Greenspun and K. S. Pister, "First leaps of an electrostatic inchworm motor-driven jumping microrobot," in *Proc. Hilton Head Solid-State Sensors, Actuators, Microsyst. Workshop*, 2018, pp. 1–4.
[31] I. Paprotny and S. Bergbreiter, "Small-scale robotics: An introduction," in *Proc. Workshop IEEE Int. Conf. Robot. Automat.*, 2013, pp. 1–15.
[32] S. Hollar, A. Flynn, C. Bellew, and K. Pister, "Solar powered 10 mg silicon robot," in *Proc. 16th Annu. IEEE Int. Conf. Micro Electro Mech. Syst.*, 2003, pp. 706–711.
[33] B. Goldberg *et al.*, "Power and control autonomy for high-speed locomotion with an insect-scale legged robot," *IEEE Robot. Automat. Lett.*, vol. 3, no. 2, pp. 987–993, Apr. 2018.
[34] A. M. Hoover, E. Steltz, and R. S. Fearing, "RoACH: An autonomous 2.4 g crawling hexapod robot," in *Proc. IEEE Int. Conf. Intell. Robots Syst.*, 2008, pp. 26–33.
[35] W. Driesen, T. Varidel, S. Regnier, and J. M. Breguet, "Micro manipulation by adhesion with two collaborating mobile micro robots," *J. Micromech. Microeng.*, vol. 15, no. 10, pp. S259–S267, 2005.
[36] W. Driesen, A. Rida, J.-M. Breguet, and R. Clavel, "Friction based locomotion module for mobile MEMS robots," in *Proc. IEEE Int. Conf. Intell. Robots Syst.*, 2007, pp. 3815–3820.
[37] N. Doshi, K. Jayaram, S. Castellanos, S. Kuindersma, and R. J. Wood, "Effective locomotion at multiple stride frequencies using proprioceptive feedback on a legged microrobot," *Bioinspiration Biomimetics*, vol. 14, no. 5, 2019, Art. no. 056001.
[38] R. St Pierre, W. Gao, J. E. Clark, and S. Bergbreiter, "Viscoelastic legs for open-loop control of gram-scale robots," *Bioinspiration Biomimetics*, vol. 15, no. 5, 2020, Art. no. 055005.
[39] P. Birkmeyer, K. Peterson, and R. S. Fearing, "DASH: A dynamic 16g hexapedal robot," in *Proc. IEEE Int. Conf. Intell. Robots Syst.*, 2009, pp. 2683–2689.
[40] S. Kim, J. E. Clark, and M. R. Cutkosky, "iSprawl: Design and tuning for high-speed autonomous open-loop running," *Int. J. Robot. Res.*, vol. 25, no. 9, pp. 903–912, 2016.
[41] A. Lipp, H. Wolf, and F. O. Lehmann, "Walking on inclines: Energetics of locomotion in the ant camponotus," *J. Exp. Biol.*, vol. 208, pp. 707–719, 2005.
[42] D. Berrigan and J. R. B. Lighton, "Energetics of pedestrian locomotion in adult male blowflies, protophormia-terraenovae (Diptera, calliphoridae)," *Physiol. Zoology*, vol. 67, no. 5, pp. 1140–1153, 1994.
[43] D. Berrigan and J. R. Lighton, "Bioenergetic and kinematic consequences of limblessness in larval diptera," *J. Exp. Biol.*, vol. 179, no. 1, pp. 245–259, 1993.
[44] J. R. B. Lighton, G. A. Bartholomew, and D. H. Feener, "Energetics of locomotion and load carriage and a model of the energy-cost of foraging in the leaf-cutting ant Atta-colombica Guer," *Physiol. Zoology*, vol. 60, no. 5, pp. 524–537, 1987.
[45] T. Jensen and I. Holm-Jensen, "Energetic cost of running in workers of three ant species, Formica fusca L., Formica rufa L., and camponotus herculeanus L. (Hymenoptera, Formicidae)," *J. Comp. Physiol.*, vol. 137, no. 2, pp. 151–156, 1980.
[46] L. Reinhardt and R. Blickhan, "Level locomotion in wood ants: Evidence for grounded running," *J. Exp. Biol.*, vol. 217, pp. 2358–2370, 2014.
[47] J. H. Fewell, J. F. Harrison, J. R. Lighton, and M. D. Breed, "Foraging energetics of the ant, Paraponera clavata," *Oecologia*, vol. 105, no. 4, pp. 419–427, 1996.

**Yifan Zhang** received the B.S. degree in material processing and control engineering from the Hefei University of Technology, Hefei, China, in 2018, and the M.S. degree in mechatronic engineering from the Harbin Institute of Technology, Shenzhen, China, in 2020.

His research interests include miniature robotics and soft robotics.

**Renjie Zhu** (Graduate Student Member, IEEE) received the B.S. degree in mechatronic engineering from the Changchun University of Science and Technology, Changchun, China, in 2017, and the M.S. degree in biomedical engineering from the Beihang University, Beijing, China, in 2020.

He is currently a Research Assistant with the Department of Mechanical and Energy Engineering, Southern University of Science and Technology, Shenzhen, China. His research interests include miniature robotics and soft robotics.

**Jianhao Wu** received the B.S. degree in mechanical engineering from the Southern University of Science and Technology, Shenzhen, China, in 2021. He is currently working toward the M.S. degree in mechanical engineering with the University of Southern California, Los Angeles, CA, USA.

His research interests include miniature robotics and mechanical design.

**Hongqiang Wang** (Member, IEEE) received the B.S. and M.S. degrees in mechanical engineering from the Xi'an Jiao Tong University, Xi'an, China, in 2008 and 2011, respectively, and the Ph.D. degree in precision mechanical engineering from the Tokyo University, Tokyo, Japan, in 2015.

He is currently an Associate Professor with the Department of Mechanical and Energy Engineering, Southern University of Science and Technology, Shenzhen, China. His research interests include miniature robotics, novel actuators, new flexible motors, soft robotics, and medical robotics.